ARTICLE

Unconventional superconductivity in magic–angle graphene superlattices

Yuan Cao[1], Valla Fatemi[1], Shiang Fang[2], Kenji Watanabe[3], Takashi Taniguchi[3], Efthimios Kaxiras[2,4] & Pablo Jarillo-Herrero[1]

The behaviour of strongly correlated materials, and in particular unconventional superconductors, has been studied extensively for decades, but is still not well understood. This lack of theoretical understanding has motivated the development of experimental techniques for studying such behaviour, such as using ultracold atom lattices to simulate quantum materials. Here we report the realization of intrinsic unconventional superconductivity—which cannot be explained by weak electron–phonon interactions—in a two-dimensional superlattice created by stacking two sheets of graphene that are twisted relative to each other by a small angle. For twist angles of about 1.1°—the first 'magic' angle—the electronic band structure of this 'twisted bilayer graphene' exhibits flat bands near zero Fermi energy, resulting in correlated insulating states at half-filling. Upon electrostatic doping of the material away from these correlated insulating states, we observe tunable zero-resistance states with a critical temperature of up to 1.7 kelvin. The temperature–carrier-density phase diagram of twisted bilayer graphene is similar to that of copper oxides (or cuprates), and includes dome-shaped regions that correspond to superconductivity. Moreover, quantum oscillations in the longitudinal resistance of the material indicate the presence of small Fermi surfaces near the correlated insulating states, in analogy with underdoped cuprates. The relatively high superconducting critical temperature of twisted bilayer graphene, given such a small Fermi surface (which corresponds to a carrier density of about 10^{11} per square centimetre), puts it among the superconductors with the strongest pairing strength between electrons. Twisted bilayer graphene is a precisely tunable, purely carbon-based, two-dimensional superconductor. It is therefore an ideal material for investigations of strongly correlated phenomena, which could lead to insights into the physics of high-critical-temperature superconductors and quantum spin liquids.

Strong interactions among particles lead to fascinating states of matter, such as quark–gluon plasmas, various forms of nuclear matter within neutron stars, strange metals and fractional quantum Hall states[1–3]. An intriguing class of strongly correlated materials is the unconventional superconductors, which includes materials with a range of superconducting critical temperatures T_c, from heavy-fermion and organic superconductors with relatively low T_c (a few to a few tens of kelvin) to iron pnictides and cuprates that can have $T_c > 100$ K (refs 4–8). Despite extensive experimental efforts to characterize these materials, unconventional superconductors are challenging to study theoretically because the models that are typically used to describe them cannot be solved exactly, motivating the development of alternative approaches for investigating and modelling strongly correlated systems. One approach is to simulate quantum materials with ultracold atoms trapped in optical lattices, although technical advances are necessary to realize d-wave superfluidity with ultracold atoms at lower temperatures than are currently possible[9,10].

Here we report the observation of unconventional superconductivity in a two-dimensional superlattice made from graphene—specifically, 'magic angle' twisted bilayer graphene (TBG). Created by the moiré pattern between the two graphene sheets, the magic-angle TBG superlattice has a periodicity of about 13 nm, between that of crystalline superconductors (a few ångström) and optical lattices (about a micrometre). One of the key advantages of this system is the *in situ* electrical tunability of the charge carrier density in a flat band with a bandwidth of the order of 10 meV. This tunability enables us to study the phase diagram of unconventional superconductivity in unprecedented resolution, without relying on multiple devices that are possibly hampered by different disorder realizations. The superconductivity that we observe has several features similar to that of cuprates, including dome structures in the phase diagram and quantum oscillations that point to small Fermi surfaces near a correlated insulator state. Furthermore, it occurs for record-low carrier densities of the order of 10^{11} cm^{-2}, orders of magnitude lower than the carrier densities of typical two-dimensional superconductors. The relatively high $T_c = 1.7$ K for such small densities puts magic-angle TBG among the superconductors with the strongest coupling, in the same league as cuprates and the recently identified FeSe thin layers[11]. Our results establish magic-angle TBG as a purely carbon-based two-dimensional superconductor and, more importantly, as a relatively simple and highly tunable material that enables thorough investigation of strongly correlated physics.

Monolayer graphene has a linear energy dispersion at its charge neutrality point. When two aligned graphene sheets are stacked, the hybridization of their bands due to interlayer hopping results in fundamental modifications to the low-energy band structure depending on the stacking order (AA or AB). If an additional twist angle is present between layers, a hexagonal moiré pattern consisting of alternating AA- and AB-stacked regions emerges and acts as a superlattice modulation[12–16]. The superlattice potential folds the band structure into the mini Brillouin zone. Hybridization between adjacent Dirac cones in the mini Brillouin zone has an effect on the Fermi velocity at the charge neutrality point, reducing it from the typical value[12–18] of 10^6 m s^{-1}. At low twist angles, each electronic band in the mini Brillouin zone has a four-fold degeneracy of spins and valleys, the latter inherited from the original electronic structure of graphene[12,17,19]. For convenience, we define the superlattice density $n_s = 4/A$ to be the density that

[1]Department of Physics, Massachusetts Institute of Technology, Cambridge, Massachusetts 02139, USA. [2]Department of Physics, Harvard University, Cambridge, Massachusetts 02138, USA. [3]National Institute for Materials Science, Namiki 1-1, Tsukuba, Ibaraki 305-0044, Japan. [4]John A. Paulson School of Engineering and Applied Sciences, Harvard University, Cambridge, Massachusetts 02138, USA.

corresponds to full-filling of each set of degenerate superlattice bands, where $A \approx \sqrt{3}\,a^2/(2\theta^2)$ is the area of the moiré unit cell, $a = 0.246$ nm is the lattice constant of the underlying graphene lattice and θ is the twist angle. In Supplementary Video, we present an animation of the way in which the band structure in the mini Brillouin zone of TBG evolves as the twist angle varies from $\theta = 3°$ to $\theta = 0.8°$, calculated using a continuum model for one valley[12].

Special angles, namely the 'magic angles', exist, at which the Fermi velocity drops to zero; the first magic angle is predicted[12] to be $\theta_{\mathrm{magic}}^{(1)} \approx 1.1°$. Near this twist angle, the energy bands near charge neutrality, which are separated from other bands by single-particle gaps, become remarkably flat. The typical energy scale for the entire bandwidth is about 5–10 meV (Fig. 1c)[12,18]. Experimentally confirmed consequences of the flatness of these bands are high effective mass in the flat bands (as observed in quantum oscillations) and correlated insulating states at half-filling of these bands, corresponding to $n = \pm n_s/2$, where $n = CV_g/e$ is the carrier density defined by the gate voltage V_g (C is the gate capacitance per unit area and e is the electron charge)[18]. These insulating states are a result of the competition between Coulomb energy and quantum kinetic energy, which gives rise to a correlated insulator at half-filling that has characteristics consistent with Mott-like insulator behaviour[18]. The doping density that is required to reach the Mott-like insulating states is $n_s/2 \approx (1.2{-}1.6) \times 10^{12}$ cm^{-2}, depending on the exact twist angle. Here we report transport data that clearly demonstrate that superconductivity is achieved as the material is doped slightly away from the Mott-like insulating state in magic-angle TBG. We observed superconductivity across multiple devices with slightly different twist angles, with the highest critical temperature that we achieved being 1.7 K.

Superconductivity in magic-angle TBG

In Fig. 1a we show the typical device structure of fully encapsulated TBG devices. The two sheets of graphene originate from the same exfoliated flake, which permits a relative twist angle that is controlled precisely to within about 0.1°–0.2° (refs 17, 20, 21). The encapsulated TBG stack is etched into a 'Hall' bar and contacted from the edges[22]. Electrical contacts are made from non-superconducting materials (thermally evaporated Au on a Cr sticking layer) to avoid any potential
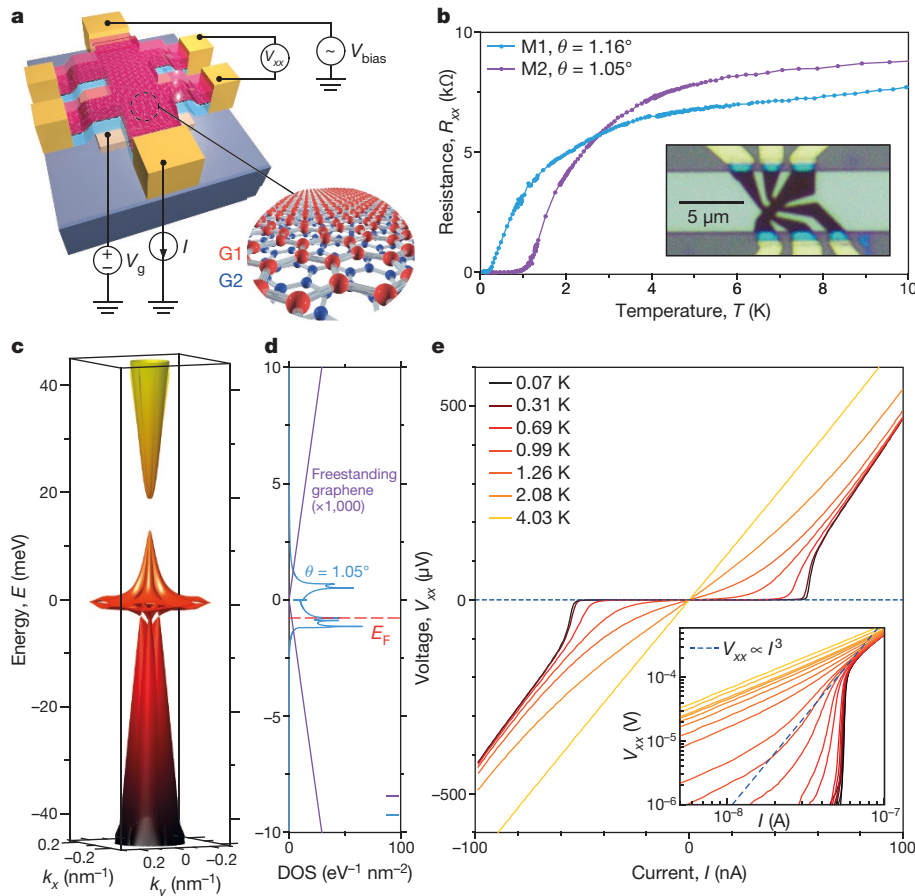
**Figure 1 | Two-dimensional superconductivity in a graphene superlattice. a**, Schematic of a typical twisted bilayer graphene (TBG) device and the four-probe (V_{xx}, V_g, I and the bias voltage V_{bias}) measurement scheme. The stack consists of hexagonal boron nitride on the top and bottom, with two graphene bilayers (G1, G2) twisted relative to each other in between. The electron density is tuned by a metal gate beneath the bottom hexagonal boron nitride layer. **b**, Four-probe resistance $R_{xx} = V_{xx}/I$ (V_{xx} and I are defined in **a**) measured in two devices M1 and M2, which have twist angles of $\theta = 1.16°$ and $\theta = 1.05°$, respectively. The inset shows an optical image of device M1, including the main 'Hall' bar (dark brown), electrical contact (gold), back gate (light green) and SiO$_2$/Si substrate (dark grey). **c**, The band energy E of TBG at $\theta = 1.05°$ in the first mini Brillouin zone of the superlattice. The bands near charge neutrality ($E = 0$) have energies of less than 15 meV.

d, The DOS corresponding to the bands shown in **c**, for energies of -10 to $+10$ meV (blue; $\theta = 1.05°$). For comparison, the purple lines show the total DOS of two sheets of freestanding graphene without interlayer interaction (multiplied by 10^3). The red dashed line shows the Fermi energy E_F at half-filling of the lower branch ($E < 0$) of the flat bands, which corresponds to a density of $n = -n_s/2$, where n_s is the superlattice density (defined in the main text). The superconductivity is observed near this half-filled state. **e**, Current–voltage (V_{xx}–I) curves for device M2 measured at $n = -1.44 \times 10^{12}$ cm^{-2} and various temperatures. At the lowest temperature of 70 mK, the curves indicate a critical current of approximately 50 nA. The inset shows the same data on a logarithmic scale, which is typically used to extract the Berezinskii–Kosterlitz–Thouless transition temperature ($T_{BKT} = 1.0$ K in this case), by fitting to a $V_{xx} \propto I^3$ power law (blue dashed line).

proximity effects. The carrier density n is tuned by applying a voltage to a Pd/Au bottom gate electrode. In Fig. 1b we show the longitudinal resistance R_{xx} as a function of temperature for two magic-angle devices, M1 and M2, with twist angles of 1.16° and 1.05°, respectively. At the lowest temperature studied of 70 mK, both devices show zero resistance, and therefore a superconducting state. The critical temperature T_c as calculated using a resistance of 50% of the 'normal'-state (non-superconducting) value is approximately 1.7 K and 0.5 K for the two devices that we studied in detail. In Fig. 1c, d we show a single-particle band structure and density of states (DOS) near the charge neutrality point calculated for $\theta = 1.05°$. The superconductivity in both devices occurs when the Fermi energy E_F is tuned away from charge neutrality ($E_F = 0$) to be near half-filling of the lower flat band ($E_F < 0$, as indicated in Fig. 1d). The DOS within the energy scale of the flat bands is more than three orders of magnitudes higher than that of two uncoupled graphene sheets, owing to the reduction of the Fermi velocity and the increase in localization that occurs near the magic angle. However, the energy at which the DOS peaks does not generally coincide with the density that is required to half-fill the bands. In addition, we did not observe any appreciable superconductivity when the Fermi energy was tuned into the flat conduction bands ($E_F > 0$). In Fig. 1e we show the current–voltage (I–V_{xx}, where V_{xx} is the four-probe voltage, as defined in Fig. 1a) curves of device M2 at different temperatures. We observe typical behaviour for a two-dimensional superconductor. The inset shows a tentative fit of the same data to a $V_{xx} \propto I^3$ power law, as is predicted in a Berezinskii–Kosterlitz–Thouless transition in two-dimensional superconductors[23]. This analysis yields a Berezinskii–Kosterlitz–Thouless transition temperature of $T_{BKT} \approx 1.0$ K at $n = -1.44 \times 10^{12}$ cm^{-2}, where, as before,

n is the carrier density induced by the gate and measured from the charge neutrality point (which is different from the actual carrier density involved in transport, as we show below).

In contrast to other known two-dimensional and layered superconductors, the superconductivity in magic-angle TBG requires the application of only a small gate voltage, corresponding to a minimal density of only 1.2×10^{12} cm^{-2} from charge neutrality, an order of magnitude lower than the value of 1.5×10^{13} cm^{-2} in LaAlO$_3$/SrTiO$_3$ interfaces and of 7×10^{13} cm^{-2} in electrochemically doped MoS$_2$, among others[24]. Therefore, gate-tunable superconductivity can be realized in a high-mobility system without the need for ionic-liquid gating or chemical doping. In Fig. 2a we show the two-probe conductance of device M1 versus n at zero magnetic field and at a 0.4-T perpendicular magnetic field. Near the charge neutrality point ($n = 0$), a typical V-shaped conductance is observed, which originates from the renormalized Dirac cones of the TBG band structure. The insulating states centred at approximately $\pm 3.2 \times 10^{12}$ cm^{-2} (which corresponds to n_s for $\theta = 1.16°$) are due to single-particle bandgaps in the band structure that correspond to filling ± 4 electrons in each superlattice unit cell. In between, there are conductance minima at ± 2 and ± 3 electrons per unit cell. These minima are associated with many-body gaps induced by the competition between the Coulomb energy and the reduced kinetic energy due to confinement of the electronic state in the superlattice near the magic angle; these gaps give rise to insulating behaviour near the integer fillings[18]. One possible mechanism for the gaps is similar to the gap mechanism in Mott insulators, but with an extra two-fold degeneracy (for the case of ± 2 electrons) from the valleys in the original graphene Brillouin zone[17,18,25,26]. In the vicinity of -2 electrons per unit cell ($n \approx -1.3 \times 10^{12}$ cm^{-2} to $n \approx -1.9 \times 10^{12}$ cm^{-2}) and at a
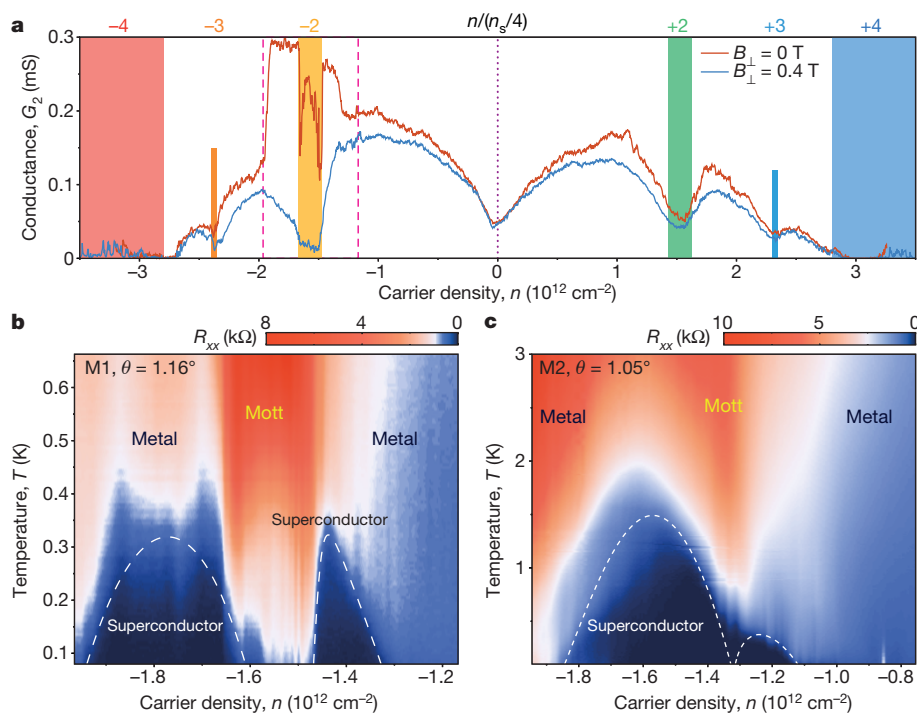

Figure 2 | Gate-tunable superconductivity in magic-angle TBG.
a, Two-probe conductance $G_2 = I/V_{bias}$ of device M1 ($\theta = 1.16°$) measured in zero magnetic field (red) and at a perpendicular field of $B_\perp = 0.4$ T (blue). The curves exhibit the typical V-shaped conductance near charge neutrality ($n = 0$, vertical purple dotted line) and insulating states at the superlattice bandgaps $n = \pm n_s$, which correspond to filling ± 4 electrons in each moiré unit cell (blue and red bars). They also exhibit reduced conductance at intermediate integer fillings of the superlattice owing to Coulomb interactions (other coloured bars). Near a filling of -2 electrons per unit cell, there is considerable conductance enhancement at zero field that is suppressed in $B_\perp = 0.4$ T. This enhancement signals the onset of

superconductivity. Measurements were conducted at 70 mK; $V_{bias} = 10 \mu$V. **b**, Four-probe resistance R_{xx}, measured at densities corresponding to the region bounded by pink dashed lines in **a**, versus temperature. Two superconducting domes are observed next to the half-filling state, which is labelled 'Mott' and centred around $-n_s/2 = -1.58 \times 10^{12}$ cm^{-2}. The remaining regions in the diagram are labelled as 'metal' owing to the metallic temperature dependence. The highest critical temperature observed in device M1 is $T_c = 0.5$ K (at 50% of the normal-state resistance). **c**, As in **b**, but for device M2, showing two asymmetric and overlapping domes. The highest critical temperature in this device is $T_c = 1.7$ K.
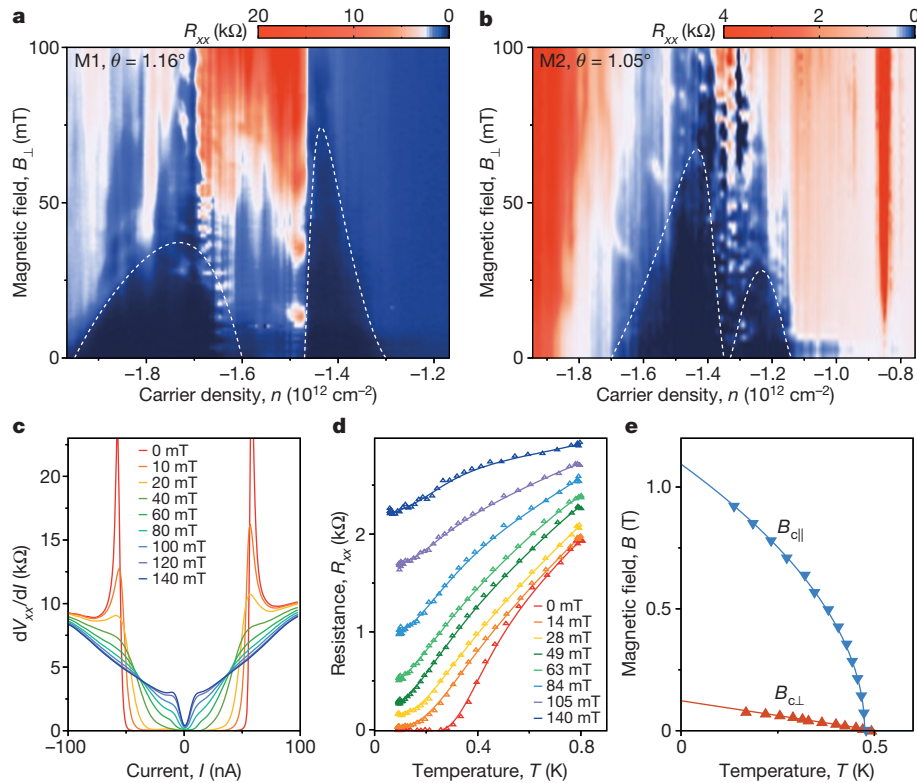
Figure 3 | Magnetic-field response of the superconducting states in magic-angle TBG. a, b, Four-probe resistance as a function of density n and perpendicular magnetic field $B_\perp$ in devices M1 (**a**) and M2 (**b**). As well as the dome structures around half-filling (similar to those in Fig. 2b, c), there are oscillatory features near the boundary between the superconducting phase and the correlated insulator phase. These oscillations are indicative of phase-coherent transport through inhomogeneous regions in the device (Methods, Extended Data Fig. 1).

c, Differential resistance dV_{xx}/dI versus d.c. bias current I for different $B_\perp$, measured for device M2. **d,** R_{xx}–T curves for different $B_\perp$, measured for device M1. **e,** Perpendicular ($B_{c\perp}$) and parallel ($B_{c\parallel}$) critical magnetic field versus temperature for device M1 (triangles; at 50% of the normal-state resistance). The fitting curves for $B_{c\perp}$ correspond to Ginzburg–Landau theory for a two-dimensional superconductor. $B_{c\parallel}$ is fitted to $B_{c\parallel}(0)(1 - T/T_c)^{1/2}$, where $B_{c\parallel}(0)$ is the parallel critical field at zero temperature. Measurements in **a**–**c** were conducted at 70 mK.

temperature of 70 mK, the conductance is substantially higher at zero magnetic field than it is in a perpendicular magnetic field of $B_\perp = 0.4$ T, consistent with mean-field suppression of a superconducting state by the magnetic field. Here, the maximum conductance is limited only by the contact resistance (Fig. 2a), which is absent in the four-probe measurements shown in the other figures.

In Fig. 2b, c we show the four-probe resistance of devices M1 and M2, respectively, as a function of density n and temperature T. Both devices show two pronounced superconducting domes on each side of the half-filling correlated insulating state. These features are similar to those associated with high-temperature superconductivity in cuprate materials. At the base temperature, the resistance inside the domes is lower than our measurement noise floor, which is more than two and three orders of magnitude lower than the normal-state resistance for devices M1 and M2, respectively. The I–V curves inside the domes display critical current behaviour (Fig. 1e), while being ohmic in the metallic phases outside the domes. Upon cooling while n is fixed at the middle of the half-filling state, the correlated insulating phase is exhibited at intermediate temperatures (from 1 K to 4 K); at lower temperatures, both devices exhibit signs of superconductivity at the lowest temperatures. Device M1 becomes weakly superconducting, whereas device M2 becomes fully superconducting. This behaviour may be explained by a coexistence of superconducting and insulating phases due to sample inhomogeneity.

Magnetic–field response

The application of a perpendicular magnetic field $B_\perp$ to a two-dimensional superconductor creates vortices that introduce dissipation and gradually suppress superconductivity[23]. In Fig. 3a, b we show the

resistance of devices M1 and M2 as a function of density and $B_\perp$. Both devices exhibit a maximum critical field of approximately 70 mT. The critical field varies strongly with doping density, showing two similar domes on each side of the half-filling state. Near the Mott-like insulating state ($n \approx -1.47 \times 10^{12}$ cm^{-2} to $n \approx -1.67 \times 10^{12}$ cm^{-2} for M1; $n \approx -1.25 \times 10^{12}$ cm^{-2} to $n \approx -1.35 \times 10^{12}$ cm^{-2} for M2), periodic oscillations of the resistance and critical current as a function of $B_\perp$ appear (see Methods and Extended Data Fig. 1 for detailed analysis). The oscillations seem to originate from phase-coherent transport through arrays of Josephson junctions, similarly to superconducting quantum interference device (SQUID)-like superconductor rings around one or more insulating islands. These junction regions could be due to slight density inhomogeneities in the devices, which would cause a few islands to be doped into the insulating phase while other parts of the device remain superconducting. Apart from these oscillatory behaviours near the boundary of the half-filling insulating state, the critical current and zero resistivity inside the domes are gradually suppressed by $B_\perp$ (Fig. 3c, d).

In Fig. 3e we show the critical magnetic field versus temperature for device M1, under perpendicular and parallel field configurations. The temperature dependence of the perpendicular critical field $B_{c\perp}$ is well described by Ginzburg–Landau theory: $B_{c\perp} = [\Phi_0/(2\pi\xi_{GL}^2)](1 - T/T_c)$, where $\Phi_0 = h/(2e)$ is the superconducting flux quantum, h is the Planck constant, and ξ_{GL} is the Ginzburg–Landau superconducting coherence length, determined from the fit to be $\xi_{GL} \approx 52$ nm at $T = 0$. On the other hand, the in-plane critical field dependence is not well explained by the Ginzburg–Landau theory for thin-film superconductors, owing to the atomic thickness of TBG (0.6 nm); at this thickness, the theory predicts an in-plane critical field of $B_{c\parallel} \geq 36$ T as the temperature
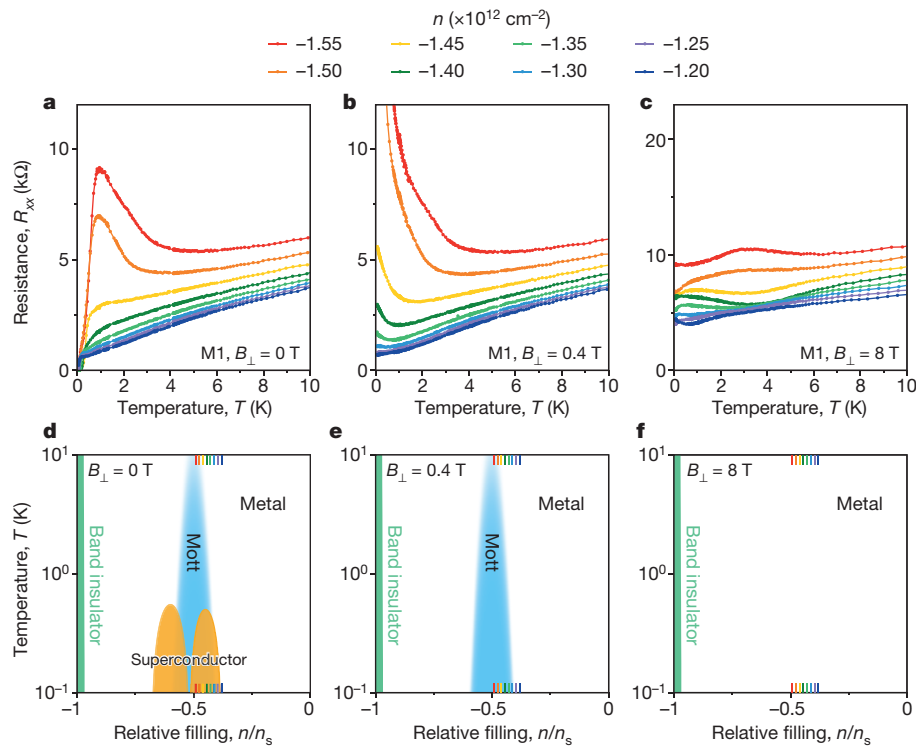
Figure 4 | Temperature–density phase diagrams of magic-angle TBG at different magnetic fields. a–c, R_{xx}–T curves for device M1 at different densities (see legend), measured in $B_\perp = 0$ T (**a**), $B_\perp = 0.4$ T (**b**) and $B_\perp = 8$ T (**c**). The magnetic field induces a superconductor–insulator–metal transition at the lowest temperatures. **d–f,** Schematic phase diagrams for the magnetic fields in **a–c**. The horizontal axis shows the relative filling n/n_s. Short coloured lines at the top and bottom of the plots denote the densities plotted in **a–c**.

approaches zero[23]. Instead, we interpret the dependence of T_c on the in-plane magnetic field $B_\parallel$ as a result of paramagnetic pair-breaking owing to the Zeeman energy. The zero-temperature in-plane critical field is extrapolated to be around 1.1 T, which is higher than but close to the value in the Pauli limit of $B_p \approx 1.85$ T K$^{-1} \times T_c \approx 0.93$ T, estimated on the basis of the Bardeen–Cooper–Schrieffer (BCS) gap formula $\Delta \approx 1.76 k_B T_c$, where k_B is the Boltzmann constant.

We note that the superconductor–metal transition in magic-angle TBG is not sharp, so extracting both B_c and T_c has some uncertainty. Qualitatively, the dependence of the in-plane critical field on temperature is $B_{c\parallel} \propto (1 - T/T_c)^{1/2}$ near T_c (ref. 27). The results described above are consistent with the existence of two-dimensional superconductivity confined in an atomically thin space. As we show in the following, the coherence length ξ is comparable to the inter-particle spacing and might suggest that the system is driven close to a crossover between a BCS-like state and a Bose–Einstein condensate (the BCS–BEC crossover).

Phase diagram of magic-angle TBG

The phase diagram of magic-angle TBG consists of correlated insulator phases and superconducting phases, which can be realized via continuous tuning of temperature, magnetic field and carrier density. Similarly to the superconducting domes discussed above, the correlated Mott-like insulator phase at half-filling also assumes a dome shape, with a transition to a metallic phase at about 4–6 K and centred around half-filling density. It has been shown[18] that the Mott-like insulator phase crosses over to a metallic phase upon application of a strong magnetic field of around 6 T either perpendicular or parallel to the devices. A plausible explanation for this crossover is that the many-body charge gap is closed by the Zeeman energy.

In Fig. 4a–c we show the resistance versus temperature data measured in device M1 at zero magnetic field, $B_\perp = 0.4$ T and $B_\perp = 8$ T, respectively. At zero field, we observe the transition from a metal at high temperatures (above 5 K) to a superconductor. Close to half-filling there

is an intermediate region in which insulating temperature dependence is observed from about 1 K to 4 K (above T_c); we identify this region as corresponding to the Mott-like insulating phase at half-filling. In a small magnetic field $B_\perp = 0.4$ T, which is above the critical magnetic field, the system remains an insulator down to zero temperature near half-filling and a metal away from half-filling. Finally, in a strong magnetic field $B_\perp = 8$ T, the correlated insulator phase is fully suppressed by the Zeeman effect and the system is metallic everywhere between $n = -n_s$ and the charge neutrality point. Our data highlight the rich phase space of metal–insulator–superconducting physics in magic-angle TBG[28]. A schematic of the evolution of the phase diagram as the magnetic field increases is shown in Fig. 4d–f.

Quantum oscillations in the normal state

We studied quantum oscillations in the entire accessible density range, including in the vicinity of the correlated insulating state at which superconductivity occurs. In Fig. 5a, b we show the Shubnikov–de Haas oscillations in longitudinal resistance R_{xx} as a function of carrier density for the hole-doped region ($E_F < 0$) for device M2. The Landau levels in a TBG superlattice typically follow $n/n_s = N\phi/\phi_0 + s$, where $\phi = B_\perp A$ is the magnetic flux that penetrates each unit cell, $\phi_0 = h/e$ is the (non-superconducting) flux quantum, $N = \pm 1, \pm 2, \pm 3, \ldots$ is the Landau-level index, $s = 0$ denotes the Landau fan that emanates from the Dirac point, and $s = \pm 1$ denote the Landau fans that result from electron-like or hole-like quasiparticles near the band edges of the single-particle superlattice bands in the mini Brillouin zone, which emanate from $\pm n_s$. The Landau levels also exhibit a four-fold degeneracy due to spins and valleys, and so the filling-factor sequence is $\pm 4, \pm 8, \pm 12, \ldots$

Unexpectedly, in addition to these expected Landau fans, we also observe a Landau fan that emanates from the correlated insulating state at $-n_s/2$. This Landau fan has $N = -1/2, -1, -3/2, -2, \ldots$ (that is, filling factors of $-2, -4, -6, -8, \ldots$) and $s = -1/2$. The superconducting dome is distinguishable in Fig. 5a directly beneath this Landau
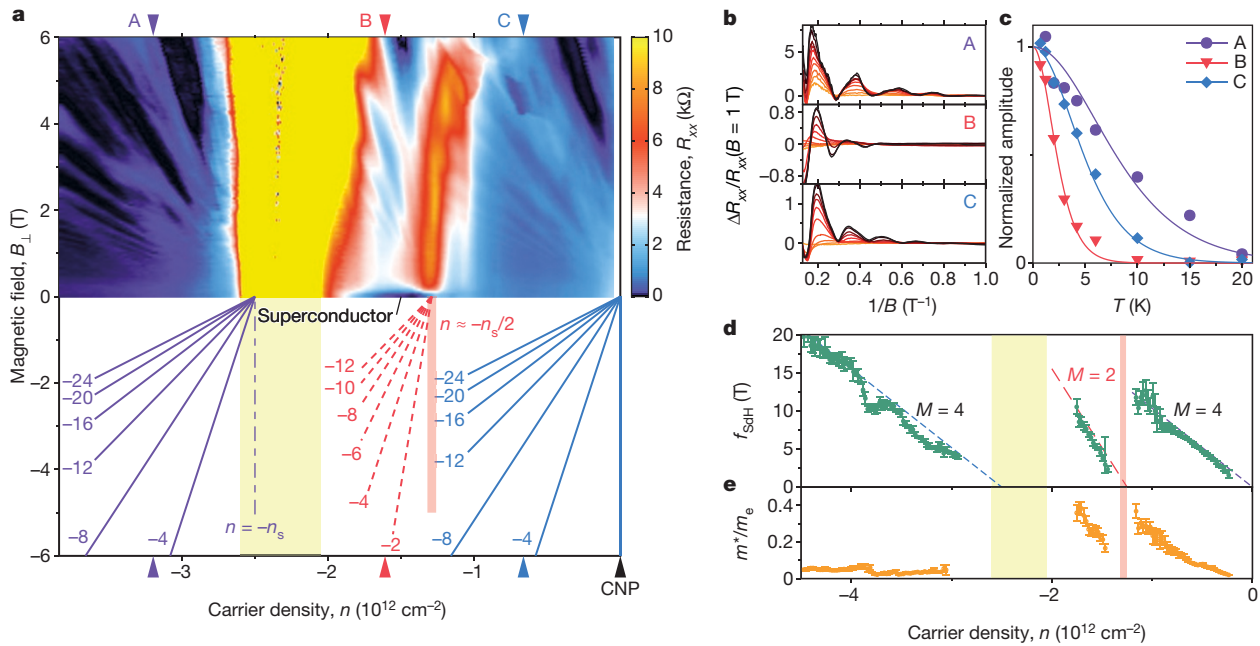
Figure 5 | Quantum oscillations in magic-angle TBG at high fields.
a, Resistance R_{xx} versus density n (hole-doped side with respect to charge neutrality) and $B_\perp$ in device M2. The lower half of the diagram shows the Landau-level structure deduced from the oscillations. The blue Landau fan, which originates from the charge neutrality point (CNP), and the purple Landau fan, which originates from the superlattice density ($n = -n_s$, yellow shaded region), illustrate the filling-factor sequences $-4, -8, -12, \ldots$ expected from the single-particle band structure with four-fold spin and valley degeneracies. The additional red fan, which originates from $-n_s/2$ (red shaded region), instead has a filling-factor sequence of $-2, -4, -6, \ldots$ that is not expected from the single-particle band structure. **b**, Temperature-dependent quantum oscillation traces $\Delta R_{xx}/R_{xx}(B = 1\,\text{T})$ at the carrier densities labelled A, B and C in **a**. From black to orange, the temperatures are 0.7 K, 1.2 K, 2.0 K, 3.0 K, 4.2 K, 6 K, 10 K, 15 K, 20 K and 30 K. **c**, Lifshitz–Kosevich fit (solid lines) of the normalized amplitudes of the oscillations shown in **b** (data points). **d**, **e**, Shubnikov–de Haas oscillation frequencies f_{SdH} and effective masses m^*/m_e as a function of carrier density n. The error bars correspond to the 90% confidence level in fitting to the Lifshitz–Kosevich formula (see Methods for definition). $M = \phi_0 \Delta n/\Delta f_{\text{SdH}}$ is the Fermi surface degeneracy.

fan, being very close to zero field and next to the correlated insulating region. Unlike commonly observed broken-symmetry states that split from a single degenerate Landau level into multiple levels, the halved filling factors appear to be intrinsic to the fan, holding down to the lowest magnetic field at which oscillations are still visible. Fractional values for s have been reported in graphene superlattices as a result of Hofstadter's butterfly, which typically occurs in much stronger magnetic fields (greater than 10 T) but becomes obvious only at the intersection of Landau levels with different integer s (refs 29–31). Therefore, the physics of Hofstadter's butterfly cannot explain the additional stand-alone fan observed here, which appears at fields as low as 1 T. Furthermore, the halving of the filling factors and s is unlikely to be explained in a non-interacting picture of unit-cell doubling due to strain or to the formation of a charge density wave, in which case either spin or valley degeneracy must be broken. We observed the same Landau level sequence in two other magic-angle TBG devices, so it is robust against small variations in twist angle and consistent across samples (Methods, Extended Data Fig. 2).

To study the non-trivial origin of the Landau fan near half-filling further, we measured the effective mass from the temperature-dependent quantum oscillation amplitude according to the Lifshitz–Kosevich formula (Methods). In Fig. 5b, c we show the oscillations and oscillation amplitudes at three different densities (indicated by arrows in Fig. 5a). In Fig. 5d, e we show the oscillation frequency f_{SdH} and the effective mass extracted by fitting the oscillation amplitudes to the Lifshitz–Kosevich formula. The dependence of f_{SdH} on carrier density n provides another perspective on the oscillations because the value of $M = \phi_0 \Delta n/\Delta f_{\text{SdH}}$ extracted from the slope $\Delta n/\Delta f_{\text{SdH}}$ provides the number of degenerate Fermi pockets M directly. The experimental data clearly fit to $M = 4$ near the charge neutrality point and for densities beyond the superlattice gap, whereas $M = 2$ for the quantum oscillations that start near the correlated insulator state and right above the

superconducting dome. The effective mass of the anomalous oscillations is about $(0.2–0.4)m_e$, where m_e is the bare electron mass. This mass is much larger than the mass near charge neutrality (about $0.1m_e$) and beyond the superlattice gap (about $0.05m_e$) at the same Δn, where Δn is density relative to the value of n at which $f_{\text{SdH}} = 0$ in Fig. 5d.

The quantum oscillations above the superconducting dome clearly indicate the existence of small Fermi surfaces that originate from the correlated insulating state, which have areas proportional to $n' = |n| - n_s/2$, rather than of a large Fermi surface with an area that corresponds to the density $|n|$ itself. The Hall measurements shown in Extended Data Fig. 3 also support this conclusion. Notably, similar small Fermi pockets that do not correspond to any pockets in the single-particle Fermi surface have been observed in underdoped cuprates, although their origin is debated[32–34]. Among the possibilities, the small Fermi surface that we observe could be the Fermi surface of quasiparticles that are created by doping a Mott insulator[6,35]. On the other hand, the halved degeneracy might be related to spin–charge separation, as predicted in a doped Mott insulator[35]. More experimental and theoretical work is needed to clarify the origin of the quantum oscillations.

Discussion

The appearance of both superconductor and correlated insulator phases in the flat bands of magic-angle TBG at such a small carrier density cannot be explained by weak-coupling BCS theory. The carrier density that is responsible for $T_c = 1.7$ K is extremely small according to the quantum oscillation measurements, merely $n' = 1.5 \times 10^{11}$ cm^{-2} at optimal doping. To place this in the context of other superconductors, in Fig. 6 we plot T_c against T_F on a logarithmic scale for various materials, where T_F is the Fermi temperature. T_F is proportional to the two-dimensional carrier density n_{2D}, which the quantum oscillations data show to be equivalent to n' for the
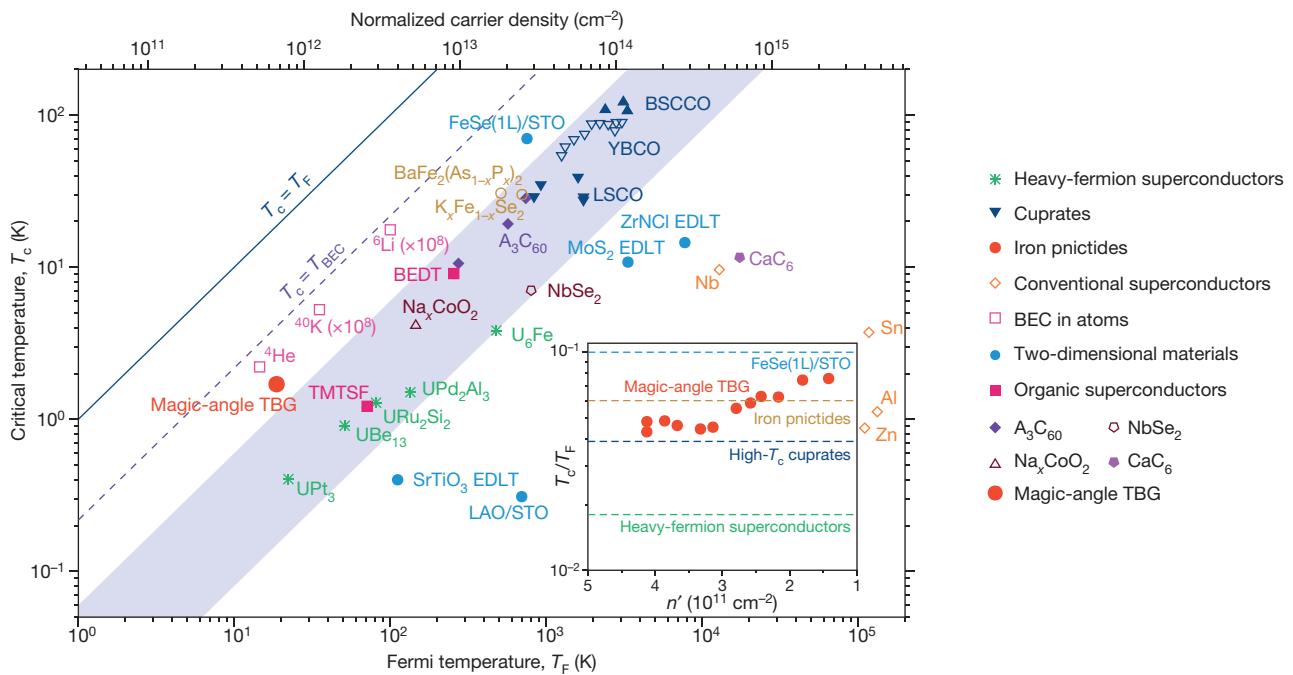
Figure 6 | Superconductivity in the strong-coupling limit. Logarithmic plot of critical temperature T_c versus Fermi temperature T_F for various superconductors[36]. The top axis is the corresponding two-dimensional carrier density n_{2D} for two-dimensional materials or $n_{3D}^{2/3}$ for three-dimensional materials, normalized by the effective mass m^*/m_e and the Fermi surface degeneracy g (and a constant factor of $1/1.52$ for the three-dimensional density). Two-dimensional superconductors are represented by filled circles; other symbols represent three-dimensional (but potentially two-dimensional-like) superconductors. For comparison, we also plot $T_{BEC} = 1.04\hbar n_{3D}/m^*$ for a three-dimensional bosonic gas (dashed line). Bose–Einstein condensation temperatures in ^{4}He, paired fermionic ^{40}K and paired fermionic ^{6}Li are shown as open pink squares[36,44] (T_c and T_F have both been multiplied by 10^8 for ^{40}K and ^{6}Li). The point for magic-

angle TBG (large red filled circle) is calculated from the two-dimensional density and the effective mass obtained from quantum oscillations (Fig. 5d, e) at the optimal doping ($n_{2D} = 1.5 \times 10^{11} \, \text{cm}^{-2}$ and $m^* = 0.2m_e$), using $g = 1$ to account for the halved degeneracy. Data for other materials are from refs 36,45–54. The blue shaded region is the approximate region in which almost all known unconventional superconductors lie. The inset shows the variation in T_c/T_F as a function of doping n' for magic-angle TBG (red filled circles). The horizontal dashed lines are the approximate T_c/T_F values of the corresponding material. YBCO, YBa$_2$Cu$_3$O$_{7-\delta}$; LSCO, La$_{2-x}$Sr$_x$CuO$_4$; BSCCO, Bi$_2$Sr$_2$Ca$_2$Cu$_3$O$_y$; LAO, LaAlO$_3$; STO, SrTiO$_3$; 1L, single layer; EDLT, electric double-layer transistor; BEDT, bisethylenedithiol; TMTSF, tetramethyltetraselenafulvalene.

superconducting dome region of magic-angle TBG[36]. Most unconventional superconductors have T_c/T_F values of about 0.01–0.05, whereas all of the conventional BCS superconductors lie on the far right in the plot, with much smaller ratios. Magic-angle TBG is located above the trend line on which most cuprates, heavy-fermion and organic superconductors lie, with a T_c/T_F value approaching that of the recently observed exotic FeSe monolayer on SrTiO$_3$ (Fig. 6 inset). This finding strongly suggests that the superconductivity in magic-angle TBG originates from electron correlations instead of weak electron–phonon coupling. One other frequently compared temperature is the Bose–Einstein condensation temperature for a three-dimensional boson gas T_{BEC}, assuming that all particles in the occupied Fermi sea pair up and condense. Cuprates and other unconventional superconductors typically have T_c/T_{BEC} ratios of roughly 0.1–0.2. The T_c/T_{BEC} ratio for magic-angle TBG is estimated to be up to 0.37, indicating very strong electron–electron interactions and possibly close proximity to the BCS–BEC crossover. This behaviour is in agreement with the fact that the coherence length in magic-angle TBG ($\xi \approx 50$ nm at optimal doping) is of the same order of magnitude as the average inter-particle distance, $(n')^{-1/2} \approx 26$ nm.

The realization of unconventional superconductivity in a graphene superlattice establishes magic-angle TBG as a relatively simple, clean, accessible and, most importantly, highly tunable material, which could be used to study correlated electron physics. The interactions in magic-angle TBG could possibly be further fine-tuned by the twist angle and by the application of perpendicular electric fields by means of differential gating[18,37]. Moreover, T_c could possibly be enhanced further by applying pressure to the graphene superlattice to increase the interlayer

hybridization or by coupling different magic-angle TBG structures to induce Josephson coupling in the vertical direction[38]. Similar magic-angle superlattices and flat-band electronic structures could also be realized with other two-dimensional materials or lattices to investigate strongly correlated systems with different properties.

Finally, despite several apparent similarities between magic-angle TBG and cuprates, there are key differences between the realizations of them. First, the valley degree of freedom in the underlying graphene lattices leads to an extra degeneracy, resulting in two carriers per superlattice unit cell at half-filling in the parent correlated insulator state. Higher quality devices and fine tuning may lead to superconductivity near the regions corresponding to one and three carriers per unit cell. Second, in magic-angle TBG the underlying superlattice is triangular, which should have a fundamental influence on the type of spin-singlet ground state it can host, owing to magnetic frustration. The lattice symmetry should also impose limitations on the possible superconducting pairing symmetry in magic-angle TBG; further experiments, for example, involving tunnelling and Josephson hetero-junctions, are required to confirm this[39]. Various pairing symmetries, including $(d + id')$-wave, $(p_x + ip_y)$-wave and spin-triplet s-wave symmetries, have been predicted theoretically in the hypothetical superconductivity of monolayer or few-layer graphene[40–42]. If the mechanism for superconductivity in magic-angle TBG is indeed related to the correlated half-filling insulating state, as is the case in $d_{x^2-y^2}$-wave cuprates, then the pairing symmetry might be chiral $(d + id')$-wave, to satisfy the underlying triangular symmetry of the superlattice. We anticipate that further experimental and theoretical work on magic-angle TBG and related magic-angle superlattices will

provide insights into the key factors that govern unconventional superconductivity, and bring us closer to realizing tunable quantum spin liquids[43].

Online Content Methods, along with any additional Extended Data display items and Source Data, are available in the online version of the paper; references unique to these sections appear only in the online paper.

1. Rajagopal, K. & Wilczek, F. in *At the Frontier of Particle Physics* (ed. Shifman, M.) Vol. 3, 2061–2151 (World Scientific, 2001).
2. v. Löhneysen, H., Rosch, A., Vojta, M. & Wölfle, P. Fermi-liquid instabilities at magnetic quantum phase transitions. *Rev. Mod. Phys.* **79**, 1015–1075 (2007).
3. Stormer, H. L. Nobel Lecture: The fractional quantum Hall effect. *Rev. Mod. Phys.* **71**, 875–889 (1999).
4. Pfleiderer, C. Superconducting phases of *f*-electron compounds. *Rev. Mod. Phys.* **81**, 1551–1624 (2009).
5. Ishiguro, T., Yamaji, K. & Saito, G. *Organic superconductors* 2nd edn (Springer, 1998).
6. Lee, P. A., Nagaosa, N. & Wen, X.-G. Doping a Mott insulator: physics of high-temperature superconductivity. *Rev. Mod. Phys.* **78**, 17–85 (2006).
7. Keimer, B., Kivelson, S. A., Norman, M. R., Uchida, S. & Zaanen, J. From quantum matter to high-temperature superconductivity in copper oxides. *Nature* **518**, 179–186 (2015).
8. Stewart, G. R. Superconductivity in iron compounds. *Rev. Mod. Phys.* **83**, 1589–1652 (2011).
9. Bloch, I., Dalibard, J. & Zwerger, W. Many-body physics with ultracold gases. *Rev. Mod. Phys.* **80**, 885–964 (2008).
10. Mazurenko, A. *et al.* A cold-atom Fermi–Hubbard antiferromagnet. *Nature* **545**, 462–466 (2017).
11. Wang, Z., Liu, C., Liu, Y. & Wang, J. High-temperature superconductivity in one-unit-cell FeSe films. *J. Phys. Condens. Matter* **29**, 153001 (2017).
12. Bistritzer, R. & MacDonald, A. H. Moiré bands in twisted double-layer graphene. *Proc. Natl Acad. Sci. USA* **108**, 12233–12237 (2011).
13. Suárez Morell, E., Correa, J. D., Vargas, P., Pacheco, M. & Barticevic, Z. Flat bands in slightly twisted bilayer graphene: tight-binding calculations. *Phys. Rev. B* **82**, 121407 (2010).
14. Moon, P. & Koshino, M. Energy spectrum and quantum Hall effect in twisted bilayer graphene. *Phys. Rev. B* **85**, 195458 (2012).
15. Fang, S. & Kaxiras, E. Electronic structure theory of weakly interacting bilayers. *Phys. Rev. B* **93**, 235153 (2016).
16. Trambly de Laissardiére, G., Mayou, D. & Magaud, L. Numerical studies of confined states in rotated bilayers of graphene. *Phys. Rev. B* **86**, 125413 (2012).
17. Cao, Y. *et al.* Superlattice-induced insulating states and valley-protected orbits in twisted bilayer graphene. *Phys. Rev. Lett.* **117**, 116804 (2016).
18. Cao, Y. *et al.* Correlated insulator behaviour at half-filling in magic-angle graphene superlattices. *Nature* **556**, https://doi.org/10.1038/nature26154 (2018).
19. Lopes dos Santos, J. M. B., Peres, N. M. R. & Castro Neto, A. H. Continuum model of the twisted graphene bilayer. *Phys. Rev. B* **86**, 155449 (2012).
20. Kim, K. *et al.* van der Waals heterostructures with high accuracy rotational alignment. *Nano Lett.* **16**, 1989–1995 (2016).
21. Kim, K. *et al.* Tunable moiré bands and strong correlations in small-twist-angle bilayer graphene. *Proc. Natl Acad. Sci. USA* **114**, 3364–3369 (2017).
22. Wang, L. *et al.* One-dimensional electrical contact to a two-dimensional material. *Science* **342**, 614–617 (2013).
23. Tinkham, M. *Introduction to Superconductivity* (Courier Corporation, 1996).
24. Saito, Y., Nojima, T. & Iwasa, Y. Highly crystalline 2D superconductors. *Nat. Rev. Mater.* **2**, 16094 (2016).
25. Mott, N. F. *Metal-Insulator Transitions* (Taylor and Francis, 1990).
26. Imada, M., Fujimori, A. & Tokura, Y. Metal-insulator transitions. *Rev. Mod. Phys.* **70**, 1039–1263 (1998).
27. Klemm, R. A. & Luther, A. Theory of the upper critical field in layered superconductors. *Phys. Rev. B* **12**, 877–891 (1975).
28. Goldman, A. M. in *BCS: 50 Years* (eds Cooper, L. N. & Feldman, D.) 255–275 (World Scientific, 2011).
29. Hunt, B. *et al.* Massive Dirac fermions and Hofstadter butterfly in a van der Waals heterostructure. *Science* **340**, 1427–1430 (2013).
30. Ponomarenko, L. A. *et al.* Cloning of Dirac fermions in graphene superlattices. *Nature* **497**, 594–597 (2013).
31. Dean, C. R. *et al.* Hofstadter's butterfly and the fractal quantum Hall effect in moiré superlattices. *Nature* **497**, 598–602 (2013).
32. Yelland, E. A. *et al.* Quantum oscillations in the underdoped cuprate YBa$_2$Cu$_4$O$_8$. *Phys. Rev. Lett.* **100**, 047003 (2008).
33. Bangura, A. F. *et al.* Small Fermi surface pockets in underdoped high temperature superconductors: observation of Shubnikov–de Haas oscillations in YBa$_2$Cu$_4$O$_8$. *Phys. Rev. Lett.* **100**, 047004 (2008).
34. Jaudet, C. *et al.* de Haas–van Alphen oscillations in the underdoped high-temperature superconductor YBa$_2$Cu$_3$O$_{6.5}$. *Phys. Rev. Lett.* **100**, 187005 (2008).
35. Kaul, R. K., Kim, Y. B., Sachdev, S. & Senthil, T. Algebraic charge liquids. *Nat. Phys.* **4**, 28–31 (2008).
36. Uemura, Y. J. Condensation, excitation, pairing, and superfluid density in high-T_c superconductors: the magnetic resonance mode as a roton analogue and a possible spin-mediated pairing. *J. Phys. Condens. Matter* **16**, S4515–S4540 (2004).
37. Gonzalez-Arraga, L. A., Lado, J. L., Guinea, F. & San-Jose, P. Electrically controllable magnetism in twisted bilayer graphene. *Phys. Rev. Lett.* **119**, 107201 (2017).
38. Yankowitz, M. *et al.* Dynamic band-structure tuning of graphene moiré superlattices with pressure. *Nature* (in the press); preprint at https://arxiv.org/abs/1707.09054 (2017).
39. Tsuei, C. C. & Kirtley, J. R. Pairing symmetry in cuprate superconductors. *Rev. Mod. Phys.* **72**, 969 (2000).
40. Nandkishore, R., Levitov, L. S. & Chubukov, A. V. Chiral superconductivity from repulsive interactions in doped graphene. *Nat. Phys.* **8**, 158–163 (2012).
41. Uchoa, B. & Castro Neto, A. H. Superconducting states of pure and doped graphene. *Phys. Rev. Lett.* **98**, 146801 (2007).
42. Hosseini, M. V. & Zareyan, M. Unconventional superconducting states of interlayer pairing in bilayer and trilayer graphene. *Phys. Rev. B* **86**, 214503 (2012).
43. Balents, L. Spin liquids in frustrated magnets. *Nature* **464**, 199–208 (2010).
44. Ku, M. J. H., Sommer, A. T., Cheuk, L. W. & Zwierlein, M. W. Revealing the superfluid lambda transition in the universal thermodynamics of a unitary fermi gas. *Science* **335**, 563–567 (2012).
45. Qian, T. *et al.* Absence of a Holelike Fermi surface for the iron-based K$_{0.8}$Fe$_{1.7}$Se$_2$ superconductor revealed by angle-resolved photoemission spectroscopy. *Phys. Rev. Lett.* **106**, 187001 (2011).
46. Hashimoto, T. *et al.* Sharp peak of the zero-temperature penetration depth at optimal composition in BaFe$_2$(As$_{1-x}$P$_x$)$_2$. *Science* **336**, 1554–1557 (2012).
47. Saito, Y., Kasahara, Y., Ye, J., Iwasa, Y. & Nojima, T. Metallic ground state in an ion-gated two-dimensional superconductor. *Science* **350**, 409–413 (2015).
48. Ye, J. T. *et al.* Superconducting dome in a gate-tuned band insulator. *Science* **338**, 1193–1196 (2012).
49. Peelaers, H. & Van de Walle, C. G. Effects of strain on band structure and effective masses in MoS$_2$. *Phys. Rev. B* **86**, 241401(R) (2012).
50. Caviglia, A. D. *et al.* Electric field control of the LaAlO$_3$/SrTiO$_3$ interface ground state. *Nature* **456**, 624–627 (2008).
51. McCollam, A. *et al.* Quantum oscillations and subband properties of the two-dimensional electron gas at the LaAlO$_3$/SrTiO$_3$ interface. *APL Mater.* **2**, 022102 (2014).
52. Ueno, K. *et al.* Electric-field-induced superconductivity in an insulator. *Nat. Mater.* **7**, 855–858 (2008).
53. Weller, T. E., Ellerby, M., Saxena, S. S., Smith, R. P. & Skipper, N. T. Superconductivity in the intercalated graphite compounds C$_6$Yb and C$_6$Ca. *Nat. Phys.* **1**, 39–41 (2005).
54. Valla, T. *et al.* Anisotropic electron-phonon coupling and dynamical nesting on the graphene sheets in superconducting CaC$_6$ using angle-resolved photoemission spectroscopy. *Phys. Rev. Lett.* **102**, 107007 (2009).

Author Contributions Y.C. fabricated samples and performed transport measurements. Y.C., V.F. and P.J.-H. performed data analysis and discussed the results. P.J.-H. supervised the project. S.F. and E.K. provided numerical calculations. K.W. and T.T. provided hexagonal boron nitride samples. Y.C., V.F. and P.J.-H. co-wrote the manuscript with input from all co-authors.

Author Information Reprints and permissions information is available at www.nature.com/reprints. The authors declare no competing interests. Readers are welcome to comment on the online version of the paper. Publisher's note: Springer Nature remains neutral with regard to jurisdictional claims in published maps and institutional affiliations. Correspondence and requests for materials should be addressed to P.J.-H. (pjarillo@mit.edu) or Y.C. (caoyuan@mit.edu).

Reviewer Information *Nature* thanks E. Mele, J. Robinson and the other anonymous reviewer(s) for their contribution to the peer review of this work.

METHODS

Sample preparation. The devices were fabricated using a modified dry-transfer technique[17,18,20]. Monolayer graphene and hexagonal boron nitride (about 10–30 nm thick) were exfoliated on SiO_2/Si chips and high-quality flakes were picked using optical microscopy and atomic force microscopy. We used a poly(bisphenol A carbonate) (PC)/polydimethylsiloxane (PDMS) stack on a glass slide mounted on a custom-made micro-positioning stage to pick up a hexagonal boron nitride flake at 90 °C, and then used the van der Waals force between hexagonal boron nitride and graphene to tear a graphene flake at room temperature. The separated graphene pieces were rotated manually by a twist angle of about 1.2°–1.3° and stacked together again, which resulted in a controlled TBG structure. The stack was encapsulated with another hexagonal boron nitride flake on the bottom and released onto a metal gate at 160 °C. We did not perform any heat annealing after this step because we found that TBG tended to relax to Bernal-stacked bilayer graphene at high temperatures. The final device geometry was defined by using electron-beam lithography and reactive ion etching. Electrical connections were made to the TBG by Cr/Au edge-contacted leads[22].

Measurements. Transport measurements were performed in a dilution refrigerator with a base temperature of 70 mK, except for the temperature-dependent quantum oscillations, which were measured in a ^{3}He fridge.

We used standard low-frequency lock-in techniques with an excitation frequency of about 5–10 Hz and an excitation current of about 0.4–5 nA. The current flowing through the sample was amplified by a current pre-amplifier and measured by the lock-in amplifier. The four-probe voltage was amplified by a voltage pre-amplifier at ×1,000 gain and measured by another lock-in amplifier.

The twist angle of the devices was determined from the transport measurements at low temperatures[18]. In brief, a rough estimate of the twist angle is provided by the carrier density of the superlattice gaps at $\pm n_s$, which present as strongly insulating states. To refine this estimate, the Landau levels that appear at high magnetic fields were fitted to the Wannier diagram, which gives the twist angle with an uncertainty of about 0.01°–0.02°.

Extracting the quantum oscillation frequency and effective mass. The effective mass in device M2 was extracted using the standard Lifshitz–Kosevich formula, which relates the temperature-dependence of resistance change $\Delta R_{xx}(T)$ to the cyclotron mass m^* (at a given magnetic field $B_\perp$):

$$\Delta R_{xx}(T) \propto \frac{\chi}{\sinh(\chi)}, \quad \chi = \frac{2\pi^2 k_B T m^*}{\hbar e B_\perp}$$

For each gate voltage (carrier density), we measured the R_{xx}–$B_\perp$ curves at different temperatures, normalized them by their low-field values and subtracted a common polynomial background in $B_\perp$. Examples of the curves are shown in Fig. 5b. The oscillation frequencies shown in Fig. 5d were extracted from these curves plotted versus $1/B_\perp$. From the temperature-dependent amplitude of the most prominent peak, we extracted m^* using the above equation (Fig. 5e). The error bars in Fig. 5d, e represent 90% confidence intervals of the fit.

Commensuration and twist angle. Mathematically, in a twisted moiré system, the lattice is strictly periodic only when the twist angle satisfies a specific relation such that lattice registration order is perfectly recovered in a finite distance. These special cases are termed 'commensurate' structures. One important parameter in commensurate TBG structures is r, which can be intuitively understood as the number of 'apparent' moiré pattern wavelengths that it takes to recover the lattice periodicity fully[19,55]. The simplest commensurate structures with $r = 1$ are called 'minimal' structures. These structures have exactly one moiré spot per unit cell. In TBG, as well as the minimal structures, which occur only at discrete angles, there are other commensurate structures that are arbitrarily close to any given angle θ with large r. However, at small twist angles, the evolution of the band structure of TBG can be viewed as semi-continuous; that is, an infinitesimal change in twist angle does not have a substantial effect on the band structure even though the lattice could be in a different family of commensurate structures (different r)[19]. In other words, the TBG system can be well approximated by a continuum model, as originally proposed in ref. 12, and the physics in minimal structures is representative of all nearby commensurate structures[12]. In our experiments, we do not expect the lattice to be in perfect commensuration, owing to disorder and intrinsic randomness due to the fabrication process. However, we think that the continuum model can faithfully represent the realistic TBG system in which any commensuration effect has been smoothed out.

We deduced the size of the moiré unit cell and the twist angle on the basis of the density of the superlattice gaps $\pm n_s$ (± 4 electrons per moiré unit cell), and then cross-checked the twist angle with the Landau levels observed at high magnetic fields. $\pm n_s$ are the only multiples of n_s that correspond to Fermi energies located within single-particle band gaps and therefore exhibit strong insulating behaviour.

For twist angles above about 0.9°–1°, the band structure at energies higher than these gaps is strongly overlapping and no single particle gaps at $\pm 2n_s$, $\pm 3n_s$, … appear[12–14,19,56]. The experimentally measured values for the single-particle insulating gaps that we observe are in the approximately 30–60-meV range[17,18]. However, below about 0.9°–1°, the superlattice gaps at $\pm n_s$ close and there is no single-particle gap at any energy in the system[21,56]. In this regime, there are Dirac-like bands that cross at $\pm 2n_s$ which might be responsible for the resistance peaks observed in devices with very small twist angles, although possible interaction effects may enhance these peaks[21]. The states observed in very-low-twist devices are clearly different from the strong insulating gaps observed here and previously[18]. There is a marked change in the band structure at about 0.9°–1° (depending on the parameters of the model being used), which leads to a transition from single-particle gaps at $\pm n_s$ to resistive states at $\pm 2n_s$. This crossover can be observed clearly in Supplementary Video, in which we show an evolution of the band structure of TBG from $\theta = 3°$ to $\theta = 0.8°$. The data in the video were calculated using the continuum model[12].

Possible effects due to finite electrical fields. It has been shown that by applying a perpendicular electrical field to Bernal-stacked bilayer graphene, topological states can emerge on the AB/BA stacking boundaries while the bulk of the AB and BA regions remains gapped[57–59]. In small-angle TBG, a similar effect can alter the band structure because the AA-stacked regions in the moiré pattern are interconnected by the AB/BA stacking boundaries. This effect has been observed recently in scanning tunnelling experiments on ultrasmall-twist-angle samples[60].

The question then arises of how the flat bands in magic-angle TBG are affected by the network of topological boundaries when a residual electrical field is present. Theoretical work on $\theta = 1.5°$ TBG has shown that when an inter-layer potential difference of $\Delta V = 300$ mV is applied the low-energy superlattice bands become even flatter and the electronic states become more localized[37]. Therefore, there is good reason to believe that the flat-band physics presented here holds even when a perpendicular electric field is present, because the electric field will probably render the band structure even more localized and correlated as the twist angle approaches the magic angle. In our experiments, we estimate that the potential difference between the two layers induced by our gate voltage is at most about 50 mV, and probably much less, owing to screening. Any possible effects of the residual electric field should be minimal.

Phase-coherent transport behaviour in superconducting magic-angle TBG. In Fig. 3a, b we observe oscillatory behaviour in the measured longitudinal resistance R_{xx} as a function of perpendicular magnetic field $B_\perp$ when the charge density is close to the boundary between the half-filling insulating state and the superconducting states. The oscillations are most clearly seen for $n \approx -1.70 \times 10^{12}\,\text{cm}^{-2}$ to $n \approx -1.60 \times 10^{12}\,\text{cm}^{-2}$ and $n \approx -1.50 \times 10^{12}\,\text{cm}^{-2}$ to $n \approx -1.47 \times 10^{12}\,\text{cm}^{-2}$ in device M1.

In Extended Data Fig. 1a, b we show the differential resistance dV_{xx}/dI versus bias current I and perpendicular magnetic field $B_\perp$. At zero bias current, the oscillations of the differential resistance with $B_\perp$ shown correspond to line cuts in Fig. 3a at densities of $n \approx -1.48 \times 10^{12}\,\text{cm}^{-2}$ (Extended Data Fig. 1a) and $n \approx -1.68 \times 10^{12}\,\text{cm}^{-2}$ (Extended Data Fig. 1b). The critical current, above which the superconductor becomes normal, oscillates with $B_\perp$ at the same frequency, as can be visualized by the bright peaks in Extended Data Fig. 1a, b. The oscillation period is $\Delta B = 22.5$ mT in Extended Data Fig. 1a and about $\Delta B = 4$ mT in Extended Data Fig. 1b.

The fact that the critical current is maximum at zero $B_\perp$ and oscillates at periodic intervals of the magnetic field suggests the existence of Josephson junction arrays—in the simplest case, a superconducting quantum interference device (SQUID)-like superconducting loop, around a normal or insulating island[23]. It is unclear whether this inhomogeneous behaviour is a result of sample disorder or a coexistence of two different phases (such as the superconducting phase and the correlated insulator phase). Owing to the two-dimensional nature of our devices, the detailed current distribution in the device cannot be uniquely determined at this moment by transport measurements; however, from the oscillation period we deduce the effective loop area of the SQUID approximately using $S = \Phi_0/\Delta B$, where $\Phi_0 = h/(2e)$ is the superconducting quantum flux. (Note the difference between $\phi_0 = h/e$ for the quantum Hall effect and $\Phi_0 = h/(2e)$ for superconductivity.) For the experimental data in Extended Data Fig. 1a, b, we obtain areas of $S = 0.09\,\mu\text{m}^2$ and $S = 0.5\,\mu\text{m}^2$, respectively. By comparison, the total device area between the voltage probes is approximately $1\,\mu\text{m}^2$.

Using a simple model of a SQUID with a phenomenological decay of the oscillation amplitude at higher magnetic fields, we attempt to reproduce the observed oscillations qualitatively using numerical simulations. In Extended Data Fig. 1c we show the simulated I–$B_\perp$ map of the differential resistance for a SQUID with area $S = 0.09\,\mu\text{m}^2$, with the same critical current $I_{c1} = I_{c2} = 7$ nA in the two branches, corresponding to the experimental data in Extended Data Fig. 1a. In Extended Data

Fig. 1d we show the simulation for an asymmetric SQUID with area $S = 0.5\,\mu m^2$ and critical currents of $I_{c1} = 6\,nA$ and $I_{c2} = 10\,nA$ for the two branches, which account for the partial cancellation of the critical current at low fields (that is, the total critical current does not reach zero in an oscillation) seen in Extended Data Fig. 1b. These simulations provide a qualitative perspective on the oscillatory phenomenon; the actual supercurrent distribution is probably much more complex and will need to be established via magnetic imaging techniques. However, our data indicate that the superconducting behaviour that we observe is indeed a phase-coherent phenomenon. Although we did not fabricate SQUID devices deliberately using magic-angle TBG, these periodic oscillations of the critical current in $B_\perp$ are probably a result of the Josephson effect through a superconductor with insulating puddles, further confirming the existence of superconductivity in magic-angle TBG.

Induced superconductivity in graphene and graphene-based systems through proximity to another superconductor has been demonstrated, and graphene-based Josephson junctions continue to be explored[61–63]. Superconductivity in graphene induced by proximity to a high-T_c superconductor has been reported recently, and indications of induced unconventional pairing have been observed[64,65].

Supplementary quantum oscillation data and low-field Hall effect. In Extended Data Fig. 2 we show magneto-transport data for device M1 and another magic-angle device D1. Both devices show evidence for the existence of an extra Landau fan with a degeneracy of $M = 2$ that emerges from the half-filling insulating states. All of the magic-angle devices that we have measured so far display quantum oscillations that correspond to emergent quasiparticles on one side of the half-filling states—the one that is away from the charge neutrality point (that is, $n < -n_s/2$ for $E_F < 0$ and $n > n_s/2$ for $E_F > 0$; see ref. 18 for the $E_F > 0$ data)—but not the other ($n > -n_s/2$ or $n < n_s/2$). The Hall measurements reported below exhibit a similar asymmetry around the half-filling state. This universally asymmetric behaviour, regardless of the twist angle, might be explained if the effective mass of the quasiparticles on the side closer to charge neutrality is much larger, and therefore the corresponding quasiparticle has a much lower mobility, so that the quantum oscillations cannot be observed and their contribution to the Hall effect becomes negligible. Further theoretical work could potentially shed more light on the true nature of the many-body energy gap and the related quasiparticles.

We determined the Fermi surface area in the magic-angle TBG devices using the Shubnikov–de Hass oscillation frequency in a magnetic field (Fig. 5). We find that oscillations emerge from the correlated insulating state at half-filling $n = -n_s/2$, and the oscillation frequency indicates small Fermi pockets associated with a shifted density of $n' = |n| - n_s/2$.

In Extended Data Fig. 3 we show another measurement of the transport carrier density via the low-field Hall effect measured up to $\pm 1\,T$. The measured Hall density, given by $n_H = -(1/e)(dR_{xy}/dB_\perp)^{-1}_{B_\perp = 0}$, provides an independent measurement of the carrier density in the system. In both devices, at a temperature of 0.4 K we observe that, whereas the Hall density follows the gate-induced density closely ($n_H = n$) near charge neutrality and up to the half-filling insulating states at $|n| = n_s/2$, it 'resets' to a much smaller value beyond $|n| = n_s/2$. The Hall density beyond these points behaves as if the charge carriers that contribute to transport are just those added beyond $|n| = n_s/2$, and roughly follows $n_H = n + n_s/2$ for $n < -n_s/2$ and $n_H = n - n_s/2$ for $n > n_s/2$. This behaviour is in agreement with the measurements of the quantum oscillation frequency shown in Fig. 5d.

This resetting effect is quickly suppressed by raising the temperature to about 10 K. Beyond this temperature the Hall density increases monotonically towards the band edge. At these higher temperatures, the Hall density in the flat bands no longer follows $n_H = n$. This could possibly be explained by the thermal energy kT being close to the bandwidth of the flat bands, in which case the Hall coefficient must take into consideration the contributions from carriers that are thermally excited into the higher-energy, highly dispersive bands, which have opposite polarity. By contrast, up to 30 K, the Hall density measured at very high densities ($|n| > n_s$) exhibits very linear behaviour according to $|n_H| = |n| - n_s$ regardless of the temperature, which is consistent with the highly-dispersive, low-mass bands above and below the flat bands, as seen in Fig. 1c.

Data availability. The data that support the findings of this study are available from the corresponding authors on reasonable request.

55. Shallcross, S., Sharma, S., Kandelaki, E. & Pankratov, O. A. Electronic structure of turbostratic graphene. *Phys. Rev. B* **81,** 165105 (2010).
56. Nam, N. N. T. & Koshino, M. Lattice relaxation and energy band modulation in twisted bilayer graphene. *Phys. Rev. B* **96,** 075311 (2017).
57. Zhang, F., MacDonald, A. H. & Mele, E. J. Valley Chern numbers and boundary modes in gapped bilayer graphene. *Proc. Natl Acad. Sci. USA* **110,** 10546–10551 (2013).
58. Vaezi, A., Liang, Y., Ngai, D. H., Yang, L. & Kim, E.-A. Topological edge states at a tilt boundary in gated multilayer graphene. *Phys. Rev. X* **3,** 021018 (2013).
59. Ju, L. *et al.* Topological valley transport at bilayer graphene domain walls. *Nature* **520,** 650–655 (2015).
60. Huang, S. *et al.* Emergence of topologically protected helical states in minimally twisted bilayer graphene. Preprint at https://arxiv.org/abs/1802.02999 (2018).
61. Heersche, H. B. *et al.* Bipolar supercurrent in graphene. *Nature* **446,** 56–59 (2007).
62. Calado, V. E. *et al.* Ballistic Josephson junctions in edge-contacted graphene. *Nat. Nanotechnol.* **10,** 761–764 (2015).
63. Bretheau, L. *et al.* Tunneling spectroscopy of Andreev states in graphene. *Nat. Phys.* **13,** 756–760 (2017).
64. Di Bernardo, A. *et al.* p-wave triggered superconductivity in single-layer graphene on an electron-doped oxide superconductor. *Nat. Commun.* **8,** 14024 (2017).
65. Perconte, D. *et al.* Tunable Klein-like tunnelling of high-temperature superconducting pairs into graphene. *Nat. Phys.* **14,** 25–29 (2018).
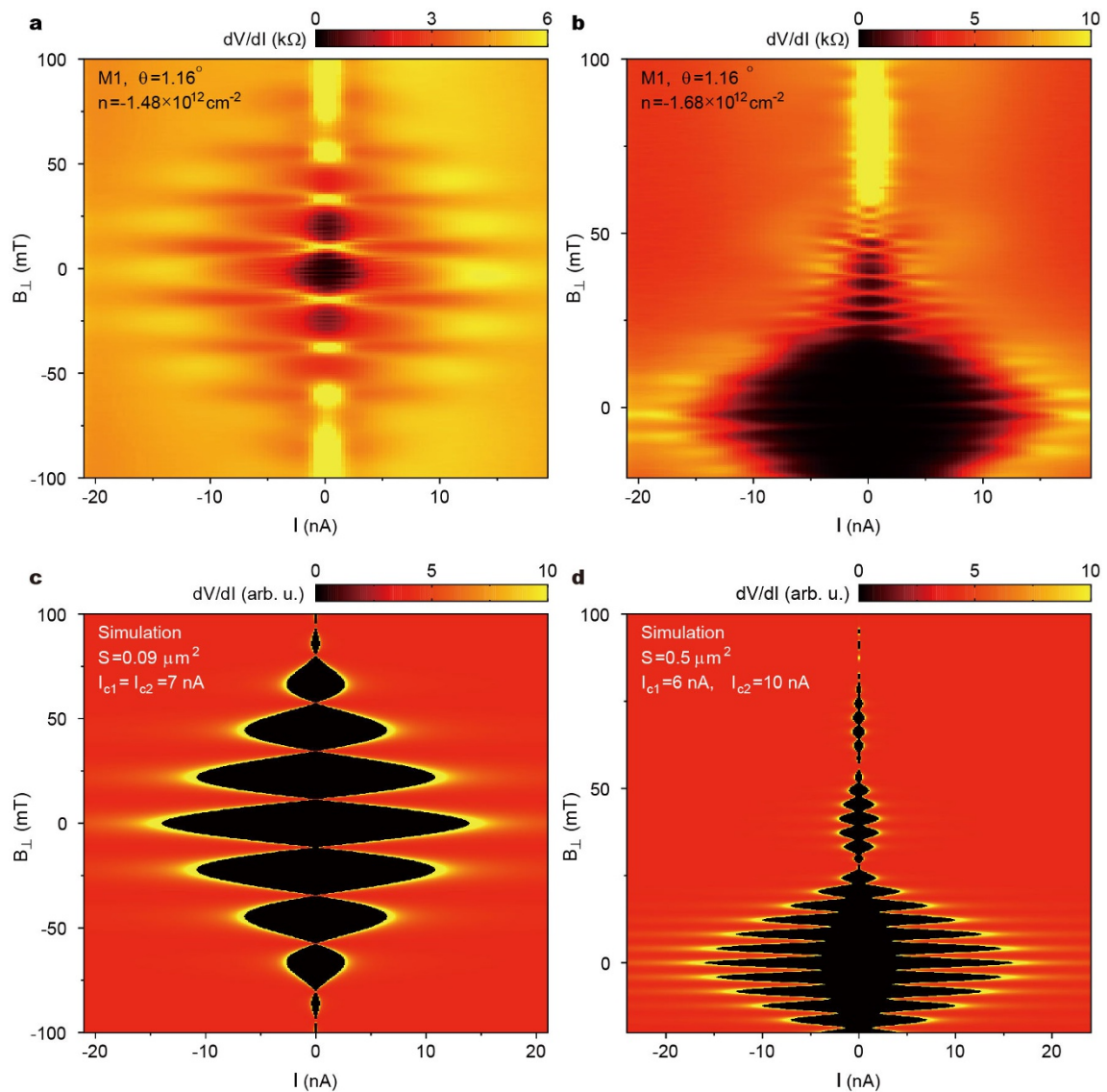
Extended Data Figure 1 | Evidence of phase-coherent transport in superconducting magic-angle TBG. a, **b**, Differential resistance dV/dI versus bias current I and perpendicular field $B_\perp$, at two different charge densities n, corresponding to those in Fig. 3a. Periodic oscillations are observed in the critical current (identified approximately as the position of the bright peaks in dV/dI). **c**, **d**, Simulations intended to reproduce qualitatively the behaviour observed in **a** and **b**.
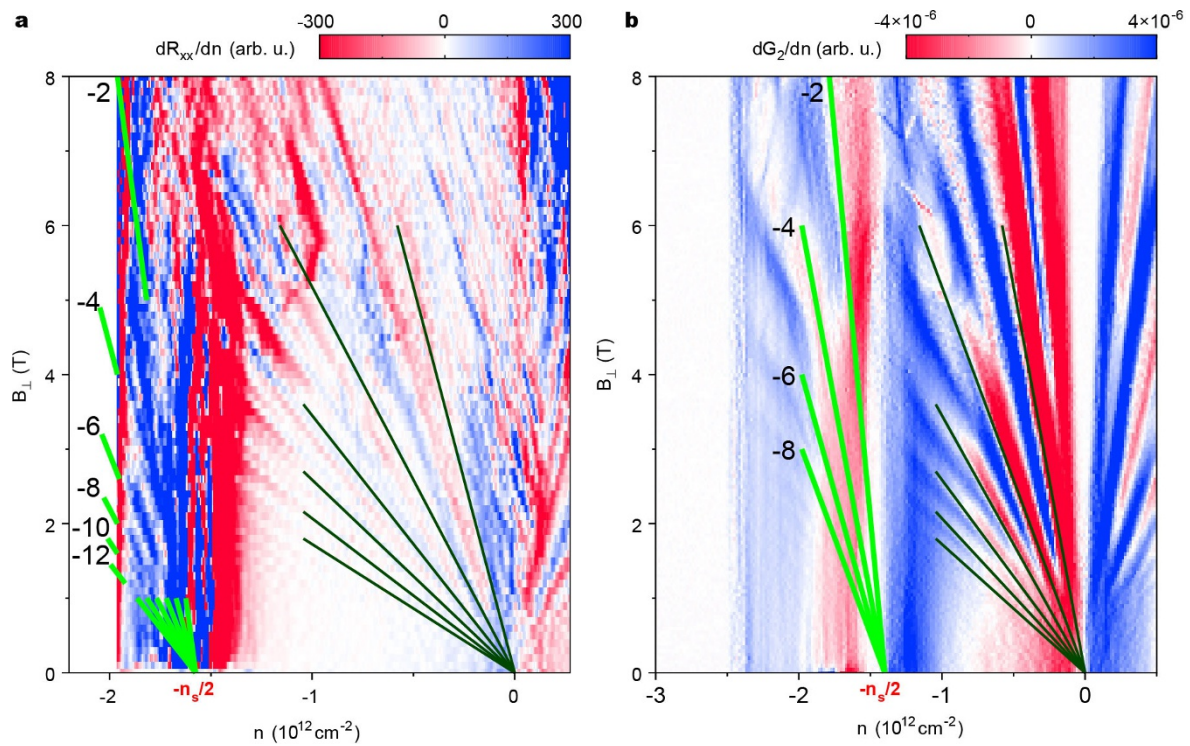
Extended Data Figure 2 | Supplementary quantum oscillation data.
a, **b**, Quantum oscillations in device M1 (**a**; $\theta = 1.16°$, data shown for R_{xx}) and device D1 (**b**; $\theta = 1.08°$, data shown for the two-probe conductance G_2). The first derivative with respect to the gate-defined charge density n has been taken in both cases to enhance the colour contrast. Both devices exhibit a Landau fan that emerges from the half-filling state $-n_s/2$ and have a Landau level sequence of $-2, -4, -6, -8, \ldots$, consistent with the results shown in Fig. 5. By comparison, the Landau fans that start from charge neutrality have a sequence of $-4, -8, -12, \ldots$
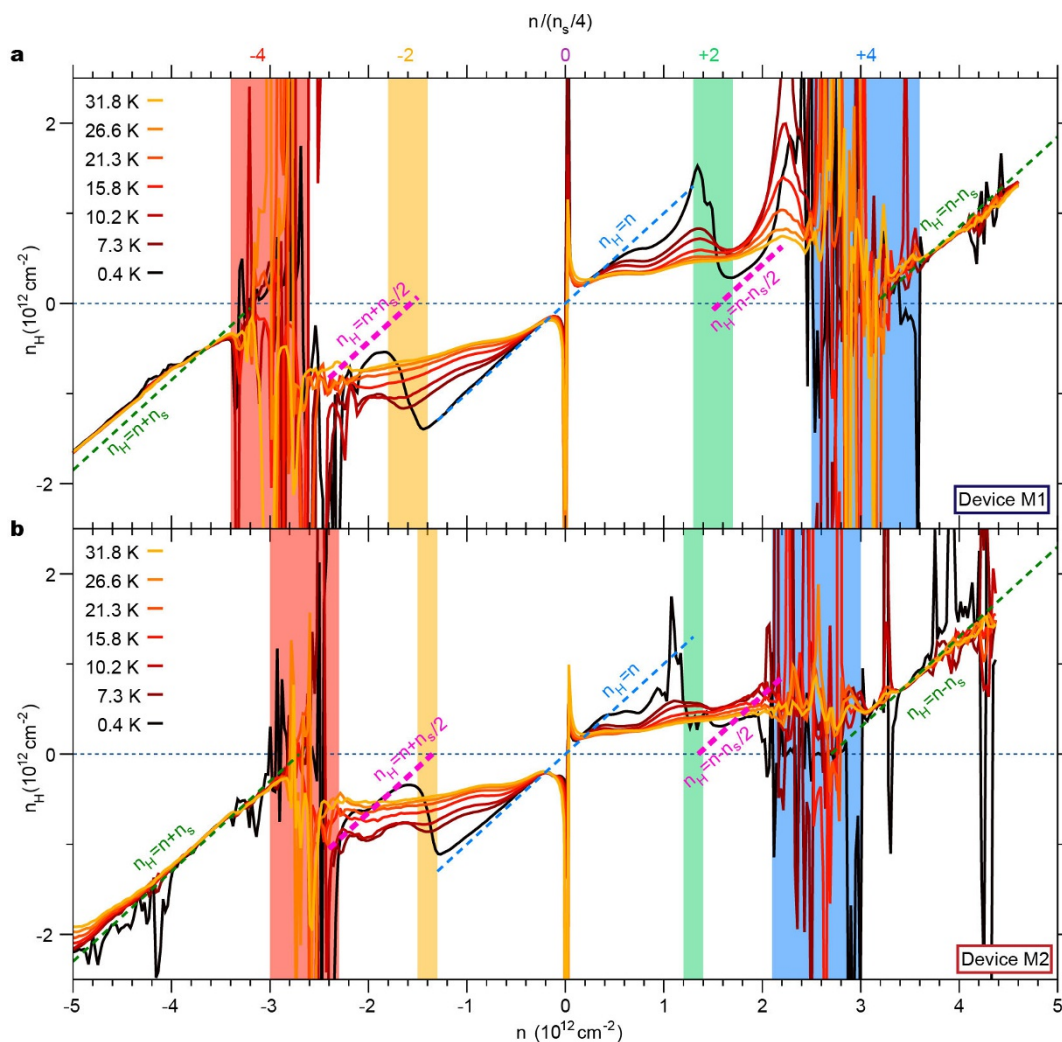
Extended Data Figure 3 | Low-field Hall effect in magic-angle TBG.
a, b, Low-field Hall effect for devices M1 (**a**) and M2 (**b**). The Hall density $n_H = -(1/e)(dR_{xy}/dB_\perp)^{-1}_{B_\perp=0}$ is plotted as a function of the total charge density induced by the gate (n), measured at temperatures from 0.4 K to 31.8 K. Coloured vertical bars correspond to densities of $-n_s$, $-n_s/2$, $n_s/2$ and n_s for the two samples. Dashed lines are the expected Hall density if the offset given in the corresponding formula is considered.